Precision Engineering 92 (2025) 219–230

Contents lists available at ScienceDirect

Precision Engineering

journal homepage: www.elsevier.com/locate/precision

Atomic insight into the speed effect on deformation mechanisms in nano-scratching of monocrystalline iron

Juan Chen [a,b], Changlin Liu [b], Hao Liu [a], Bi Zhang [a,*], Suet To [b,c,**]

[a] Department of Mechanical and Energy Engineering, Southern University of Science and Technology, Shenzhen, 518055, China
[b] State Key Laboratory of Ultraprecision Machining Technology, Department of Industrial and Systems Engineering, The Hong Kong Polytechnic University, Hung Hom, Kowloon, Hong Kong, China
[c] The Hong Kong Polytechnic University Shenzhen Research Institute, Shenzhen, China

ARTICLE INFO

Handling Editor: Dr. Masonori Kunieda

Keywords:
Deformation mechanism
Ultra-high-speed machining
Dislocation
Nano-scratching
Molecular dynamics simulation

ABSTRACT

Ultra-high-speed machining offers significant potential to enhance material removal efficiency and reduce subsurface damage in metals. However, the interplay between machining temperature and speed on dislocation evolution and subsurface damage remains inadequately understood. This study employs molecular dynamics simulations to investigate surface and subsurface deformation mechanisms in iron across various machining speeds. Results indicate that increased machining speed improves material removal efficiency. The high strain zone concentrates near the machined surface and decreases with depth, while higher machining speeds further confine shear strain to a smaller region. Specifically, the decreased dislocation length at high machining speed indicates a deformation mechanism shift dominated by the strain rate effect. Additionally, subsurface damage depth decreases with higher speeds due to reduced shear strain penetration and enhanced stress relaxation. These findings contribute to the development of low-damage machining techniques for iron and other difficult-to-machine metals within a wide speed range.

1. Introduction

Ferrous metals, such as iron, chromium, manganese, and their alloys, are extensively used across industries due to their outstanding mechanical properties and abundant reserves. Among materials used in ultra-precision machining, diamond stands out as a frequently chosen tool material due to its superior hardness and toughness [1,2]. However, the application of diamond tools in machining ferrous metals faces significant challenges, primarily due to severe tool wear and a consequent decline in machining quality [3,4]. To address this issue, researchers have dedicated considerable efforts to assess and enhance the capabilities of diamond machining for cutting ferrous metals. Early research has explored technological measures aimed at enhancing the quality and efficiency in the machining of pure iron and other ferrous metal materials. Examples include auxiliary techniques such as gas protection turning [5], cryogenic turning [6], surface modification turning [7], and ultrasonically-assisted turning [8,9], which have shown potential in suppressing tool wear and enhancing machined surface quality. Despite these advancements, the machining of ferrous metals with diamond tools remains challenging, particularly in meeting the requirements of surface quality and machining efficiency in practical applications.

Recent years have seen ultra-high-speed machining emerge as a promising approach for cutting difficult-to-machine materials. Studies have revealed that increasing the machining speed is beneficial for improving the surface quality and suppressing subsurface damage [10]. Zhang et al. [11] highlighted that at higher strain rates, machining damage tends to be confined to the surface layer, which is attributed to the "skin effect". This observation lays the theoretical groundwork for the advancement of ultra-high-speed grinding technologies, which have been demonstrated in metals, ceramics, and composite materials in previous studies. Guo et al. [12] analyzed the subsurface damage in ultra-high-speed grinding of Al6061T6 alloy. They found that the dynamic recrystallization zone, which is a type of machining-affected layer caused by intense plastic deformation, considerably decreases in depth with increasing grinding speed because of the elevated strain-rate field

* Corresponding author.
** Corresponding author. State Key Laboratory of Ultraprecision Machining Technology, Department of Industrial and Systems Engineering, The Hong Kong Polytechnic University, Kowloon, Hong Kong.
E-mail addresses: zhangb@sustech.edu.cn (B. Zhang), sandy.to@polyu.edu.hk (S. To).

https://doi.org/10.1016/j.precisioneng.2024.12.006
Received 14 June 2024; Received in revised form 14 November 2024; Accepted 5 December 2024
Available online 6 December 2024

and the lowered thermal-affected layer depth. Besides, it is reported by Li et al. [13] that the subsurface damage depth of glass-ceramics decreased with the increase of wheel speeds at three different grinding stages due to the greater material resistance to micro-crack initiation and less time for crack propagation at higher speeds. Furthermore, Guo et al. [14] revealed that the subsurface damage layers are thinner during high-speed grinding of Al/SiCp metal matrix composites compared to low-speed grinding, and the surface integrity is improved as a result of reduced material property discrepancies between the Al metal matrix and SiC particle at high speeds. Owing to the less contact duration and localized machining damage near the surface, ultra-high-speed machining has the potential in the diamond grinding of ferrous metals with minimal subsurface damage and tool wear. However, to the best of the authors' knowledge, a rare study has been reported on ultra-high-speed machining of ferrous metal using diamond abrasives, and the in-depth mechanisms involved in the material removal process and the subsurface damage during high strain rate deformation remain unexplored.

In ultra-precision machining, the material removal thickness decreases into the nanoscale and the physical variables during deformation are difficult to observe experimentally [15]. Molecular dynamics (MD) simulations have powerful implement for elucidating the deformation mechanisms of large strain rates at the nanoscale. It facilitates insights into surface generation and the microstructure evolution during machining, such as dislocation [16] and phase transformation [17]. Previous studies have investigated various aspects of nanoscale machining with the assistance of MD simulation. For example, Liu et al. [18] conducted MD nano-cutting simulations of single-crystal silicon and analyzed the reduction in amorphous layers and subsurface damage at a range of temperatures, and reported findings that aligned with experimental data. Fan et al. [19] explored the work-hardening effect of nickel-based alloy by MD simulation, focusing on dislocation and stacking fault dynamics during machining. Fang et al. [20] employed MD simulations to investigate the deformation mechanism of single-crystal gallium arsenide during nano-machining, in which the dislocation distribution, phase transformation, and amorphization were analyzed. For the speed effect, Li et al. [21] explored the influence of speed on subsurface damage and surface integrity in single-crystal silicon using MD simulation by analyzing chips and dislocations, they claimed that the higher grinding velocities increase chip volume due to accelerated phase transition from alpha-to beta-silicon by a high hydrostatic pressure. Additionally, they established an analytical model to calculate the hydrostatic stress and von Mises stress, which provides insights into the subsurface damage. Guo et al. [22] conducted MD simulations of nano-grinding on single-crystal silicon at various grinding speeds to study the subsurface damage. The results showed that the thickness of the subsurface layer increased and then decreased with the machining speed, but this was not continuous. Besides, the simulation revealed the formation of the Si-II phase and the distribution of residual stress within the subsurface layer. Zhang et al. [23] revealed the transition of failure mode with various speeds during the machining of single-crystal silicon based on MD simulation. Zhao et al. [24] reported that the temperature in the subsurface layer increases with machining speed during nano-grinding of single-crystal silicon. While in the work of Li et al. [25], higher machining speed with a critical machining angle tends to generate more chips and reduce subsurface damage during nanoscale machining of single-crystal copper. These above studies provided insights into the speed effect on material removal mechanisms. However, rare simulations for the machining mechanism of iron have been conducted. The coupling effect of temperature and machining speed on dislocation evolution and subsurface damage remains unclear and requires further in-depth exploration.

In this study, MD simulations of nano-scratching were conducted on iron workpieces to elucidate the speed effects on surface generation and subsurface damage. To analyze surface generation and the material removal process, the pile-up ratio, elastic recovery, shear strain, cutting forces, and coefficient of friction were examined across different machining speeds. Additionally, the evolution of dislocation and subsurface damage were discussed with a focus on the roles of temperature, shear strain, and internal stress. This study aims to offer insights into the deformation and material removal mechanisms of iron, potentially enhancing understanding of the speed effect on the deformation behavior.

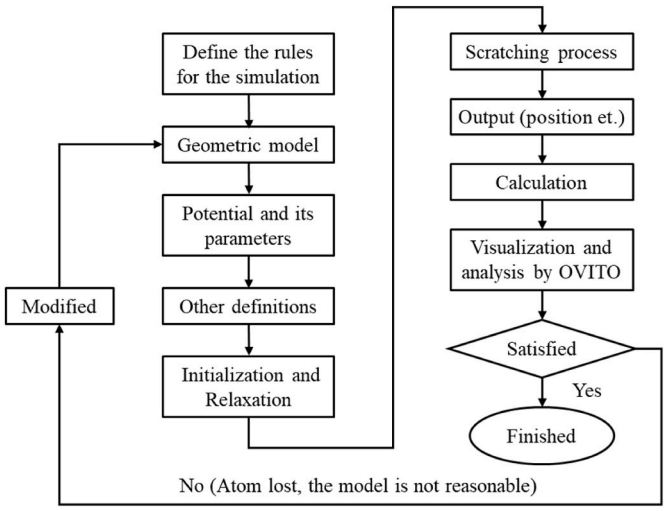

Fig. 1. Flow chart of the nano-scratching simulation process.

2. Simulation method

In this study, MD simulations were performed utilizing the Large-scale Atomic/Molecular Massively Parallel Simulator (LAMMPS) [26]. Visualization and analysis of the output data are facilitated by OVITO [27]. Fig. 1 shows the flowchart of the nano-scratching simulation process, which outlines the key steps in the MD simulations. After defining the rules such as the units, dimensions, and boundary for the simulation, the geometric model could be set based on the atom information and positions. The nano-scratching model features the cutting tool as a rigid body and the α-Fe monocrystalline workpiece as deformable, as depicted in Fig. 2. The workpiece includes three types of atoms: boundary, thermostat, and Newtonian atoms. The initial positions of the atoms were assigned based on the crystal structure of iron (body-centered cubic, BCC) by LAMMPS. Prior to the scratching simulation, atoms were relaxed in the isothermal-isobaric (NPT) ensemble at 300 K and 0 GPa. The balanced positions and velocities of atoms were obtained by performing time integration on the Nose-Hoover style non-Hamiltonian equations of motion [28]. The nano-scratching simulation was conducted along the (010) [$\bar{1}$ 00] direction. During the nano-scratching simulation, the boundary atoms are fixed in their balanced position to ensure the workpiece stability. The Newtonian atoms follow Newton's second law of motion under the microcanonical (NVE) ensemble, in which the system was allowed to evolve without any external influences, conserving the system's total energy, volume, and atom count. While the thermostat atoms are maintained at a constant temperature to dissipate heat using the canonical (NVT) ensemble by employing the Nosé-Hoover thermostat to control the temperature in a constant volume. The fixed boundary condition is used in the x and z dimensions while the periodic boundary condition is used in the y dimension to minimize the edge effects.

Adopting an accurate potential function is crucial to ensure the accuracy of MD simulation. According to previous research [29,30], the interaction between tool and workpiece atoms (Fe-C) was modeled using the Lennard-Jones potential [31] with a cutoff radius of 4.2 Å, as it effectively models the van der Waals forces and short-range repulsive

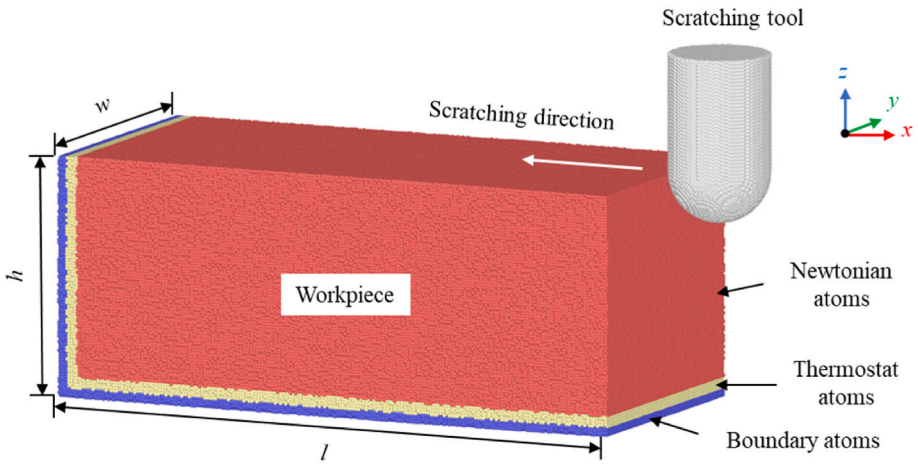

Fig. 2. MD simulation model of the nano-scratching process.

Table 1
Detailed parameters of the MD simulation.

Parameters	Value
Workpiece size ($l \times w \times h$)	60 × 28 × 24 nm
Number of workpiece atoms	About 3.49 million
Tool radius	5 nm
Scratching depth	4 nm
Scratching distance	54 nm
Machining speed	50, 100, 200, 320, 500 m/s
Timestep	1 fs

interactions in such systems. The Fe-Fe interactions are described by the embedded atom method (EAM) potential [32], which is commonly applied to computing atomic pair interactions in metal alloys and has been proven to be a robust selection in the prediction of the normal plastic behavior of iron [33,34]. The C-C interactions among tool atoms are ignored as the diamond tool is designed as a rigid body. The simulation parameters are detailed in Table 1.

3. Simulation results

3.1. Surface generation

The pile-up of the workpiece material is a critical process during surface formation [35,36]. Fig. 3 depicts the snapshots of the workpiece surface at different machining speeds. Accumulation of workpiece atoms in front of the cutting tool results in the formation of chips. While a symmetrical accumulation of workpiece atoms is observed on both sides of the tool path above the uncut surface, which can be identified as the side flow. As the machining speed increases, smooth morphology of side flow can be observed on the uncut surface, indicating a more stable piling up process at higher machining speed. Furthermore, Fig. 4 illustrates the variation of pile-up ratio at different machining speeds, which can be defined as the proportion of piled atoms (including both chips and side flow) to the theoretical removal atoms. The rise of the pile-up ratio with increasing machining speed suggests that more workpiece atoms be piled up into chips and side flow.

In addition to the piling up, workpiece material can be compressed into the surface workpiece. After machining, these atoms tend to return to their original positions to release strain energy, which could be identified as elastic recovery (ER) or the swelling effect [35,37]. Fig. 5 (a) presents the morphology of the ER layer (in red color) and the number of atoms in the ER layer at different machining speeds were counted, as shown in Fig. 5(b). A rise of the atoms in the ER layer can be observed as the machining speed increases. This variation can be explained that a longer contact duration between the tool and workpiece at lower machining speeds results in more holding time for the workpiece to be affected by the scratching tool, and the suitable increase in holding time could reduce the amount of elastic recovery [38]. Besides, as the temperature increases with the machining speeds, excessive heat accumulation leads to notable swelling marks on the machined surface

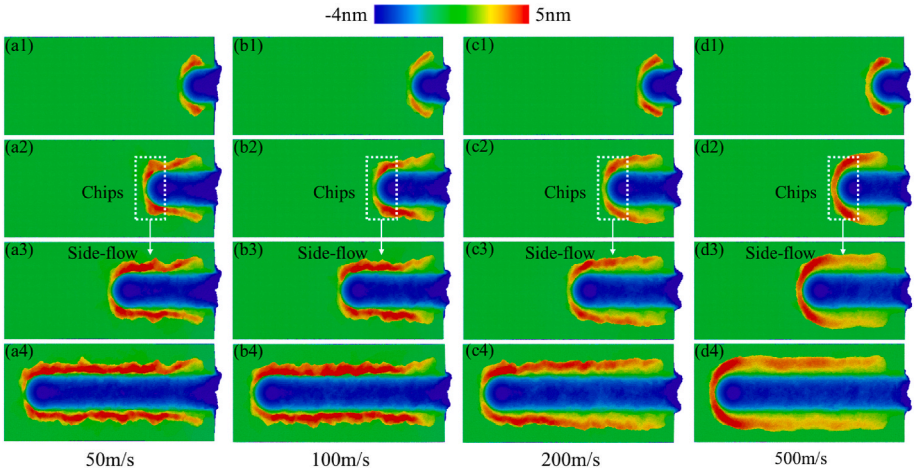

Fig. 3. Diagram of the surface generation process. (a) to (d) correspond to machining velocities with 50 m/s, 100 m/s, 200 m/s and 500 m/s. "1" to "4" correspond to scratching distances of 9 nm, 19 nm, 29 nm, and 54 nm.

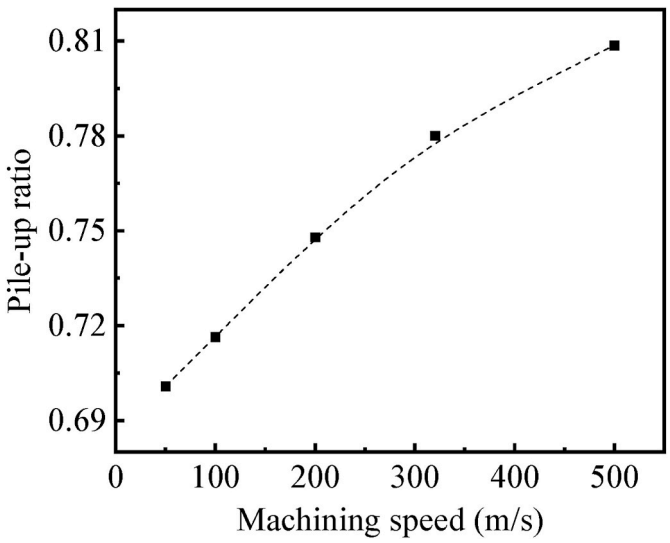

Fig. 4. Pile-up ratio at different machining speeds as the scratching distance reaches 54 nm.

[39,40]. However, as the machining speed increases to 500 m/s, the number of atoms in the ER layer slightly decreases. This could be because the swelling effect weakens as the temperature rises to the critical point of the body-centered cubic (BCC) -to face-centered cubic (FCC) phase transition, where this phase transition results in a reduction in volume.

3.2. Material removal behavior

For ferrous metal, plastic deformation occurs due to excessive shear strain during the machining process. Fig. 6 shows the snapshots of the shear strain distribution at various machining speeds. The high strain zone mainly concentrates near machined surfaces and decreases with increasing depth from the workpiece surface. As the machining speed increases, the shear strain in the depth direction gradually decreases, which means that the shear deformation is confined to the smaller region in the workpiece. This phenomenon is also recognized as the "skin effect" at the macroscopic scale [11], which has been demonstrated in metal and composite materials [12,14]. The characteristic contributes to a shallower deformation layer when machining at a higher speed, which is beneficial for suppressing subsurface damage.

Cutting force is an important indicator in demonstrating the material removal behavior. Fig. 7 illustrates the impact of machining speed on the normal force and tangential forces during the scratching process. As

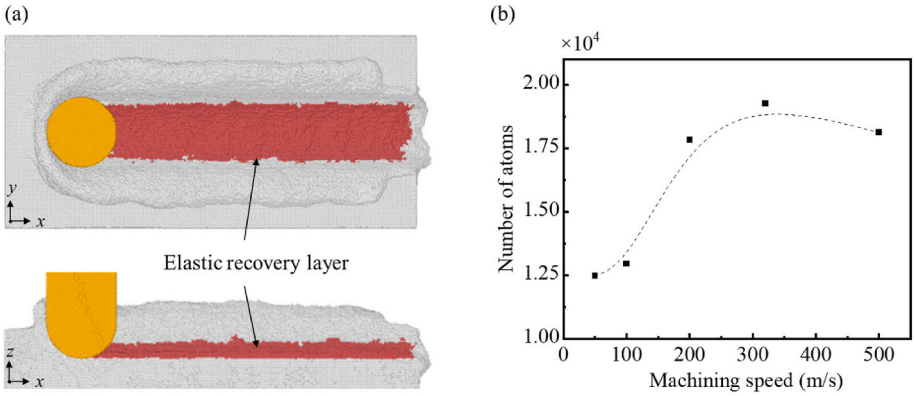

Fig. 5. (a) Snapshots of the Elastic recovery layer (in red color) on the workpiece at a machining speed of 500 m/s, (b) Number of atoms in the elastic recovery layer at different machining speeds. (For interpretation of the references to color in this figure legend, the reader is referred to the Web version of this article.)

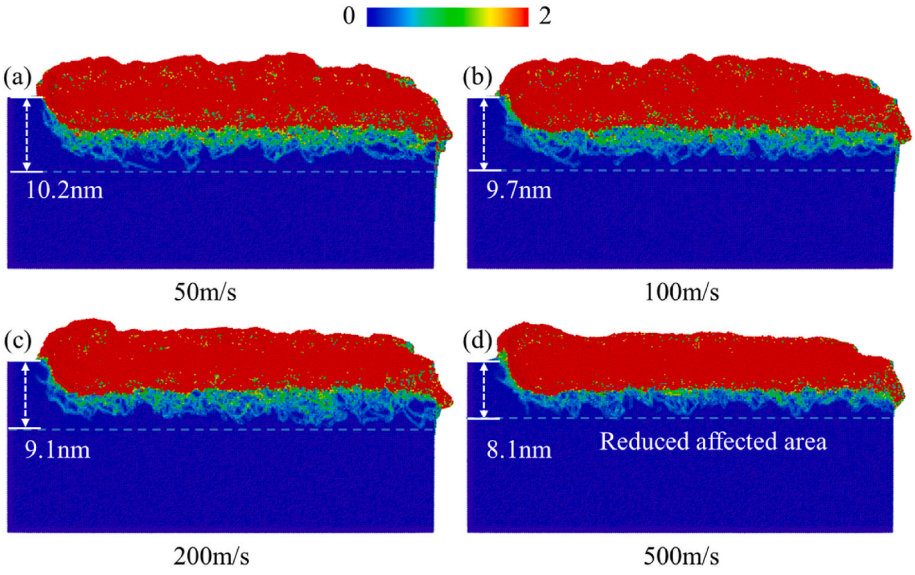

Fig. 6. Shear strain distribution diagram of the workpiece at a speed of (a) 50 m/s, (b) 100 m/s, (c) 200 m/s, and (d) 500 m/s.

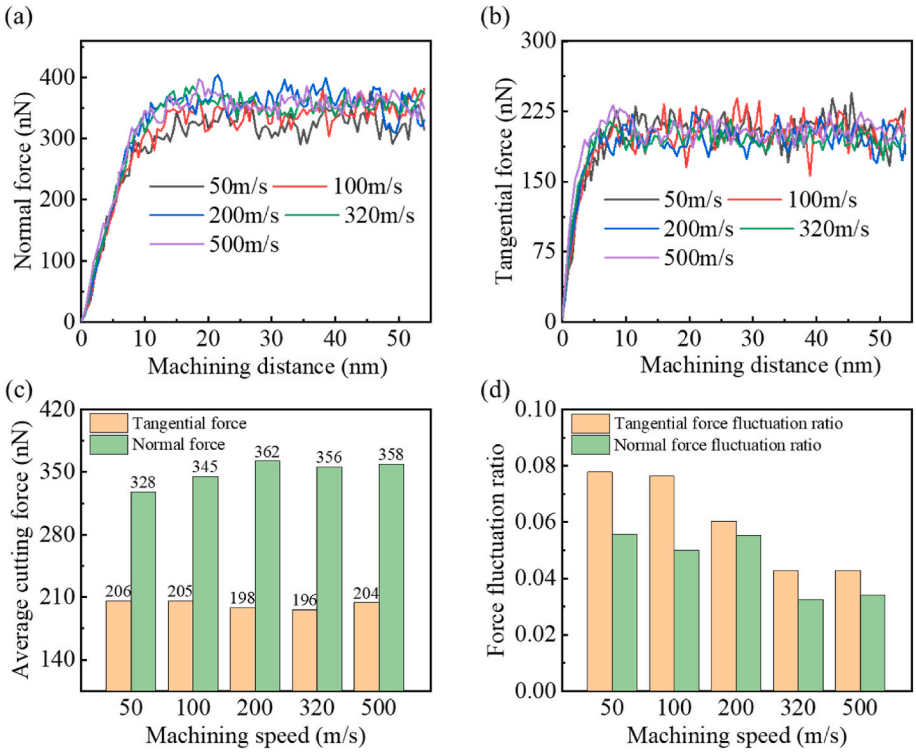

Fig. 7. Variation of (a) normal force and (b) tangential force at various machining distances, (c) average normal force and tangential force in the steady state at various machining speeds, and (d) force fluctuation ratio at different machining speeds.

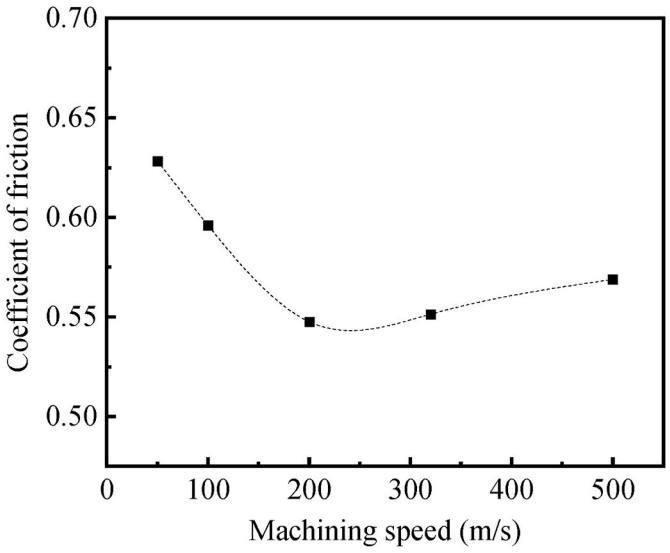

Fig. 8. Variation in coefficient of friction at various machining speeds.

illustrated in Fig. 7(a) and (b), the normal and tangential forces sharply increase at the initial machining stage due to an increase in the contact region between the tool and the workpiece. As the cutting tool advances, the cutting forces fluctuate around a stable value after a scratching distance of approximately 20 nm, indicating a steady state of the scratching process. Fig. 7(c) shows the variation in average cutting force in the steady state across various machining speeds. The average normal force increases as the speed rises from 50 m/s to 200 m/s, followed by a slight fluctuation as the speed increases further. To better reveal the extent of force fluctuation during the machining process at different speeds, the standard deviation of force over various scratching distance was calculated to obtain the force fluctuation ratio, which is defined as the ratio of the standard deviation to the mean force. Fig. 7(d) illustrates that the normal and tangential force fluctuation ratio at machining speeds higher than 200 m/s decreases compared to that at lower speeds, which indicates the reduction of cutting force fluctuation that contributes to the uniformity of the side flow pattern. Furthermore, Figs. 7(c) and 8 illustrate that both the average tangential force and the average coefficient of friction (COF) initially decrease and then show a slight increase as the machining speed increases. This phenomenon could be attributed to the coupling effects of temperature and strain rate dynamics. When the machining speed increases, thermal softening induced by elevated temperatures at higher machining speeds is advantageous for reducing the frictional resistance between the tool and the workpiece. On the other hand, the increase of the COF at 500 m/s can be ascribed to the strain-hardening effect [39]. This coupled phenomenon indicates that managing the balance between applied mechanical strain and generated heat is crucial for controlling the magnitude and characteristics of the scratching force, which is essential for optimizing the processing conditions to achieve the desired surface.

3.3. *Subsurface damage*

Subsurface damage is an important factor in the evaluation of the machining quality. Fig. 9 shows the snapshots of the subsurface damage layer (SDL) at various speeds, where the lattice structure of workpiece atoms is determined using common neighbor analysis (CNA). Atoms in body-centered cubic (BCC) structures are hidden for a clear view of the crystal defects. Dislocations, vacancies, and interstitial atoms are observed beneath the machined surface after machining. As the machining speed rises from 50 m/s to 500 m/s, the subsurface damage depth decreases from 22.4 nm to 10.8 nm. Additionally, more atomic clusters are formed within the workpiece when the machining speed increases due to the annihilation of dislocations. The formation of these point defects involves the migration of workpiece atoms, with some integrating into the perfect lattice structure as interstitial atoms and others creating vacancies at their original positions [41]. In contrast to

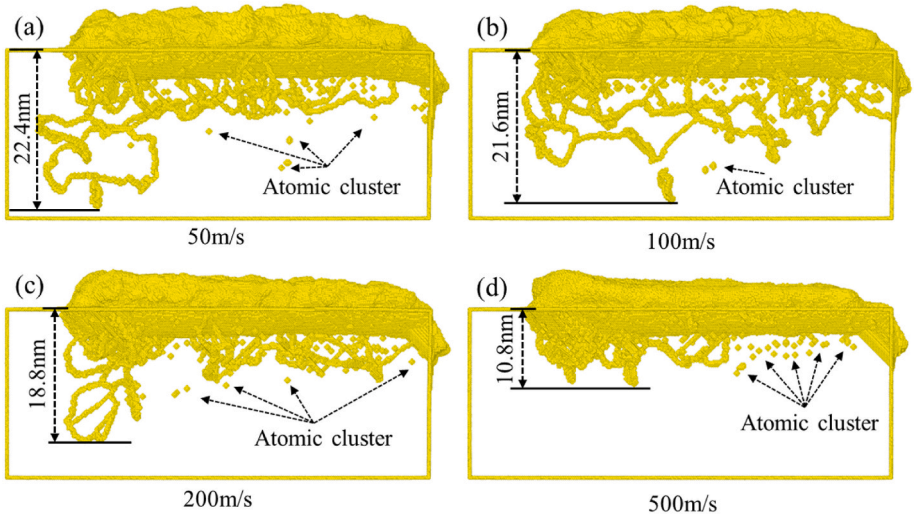

Fig. 9. Diagram of subsurface damage layer at a scratching distance of 49 nm with a speed of (a) 50 m/s, (b) 100 m/s, (c) 200 m/s, and (d) 500 m/s.

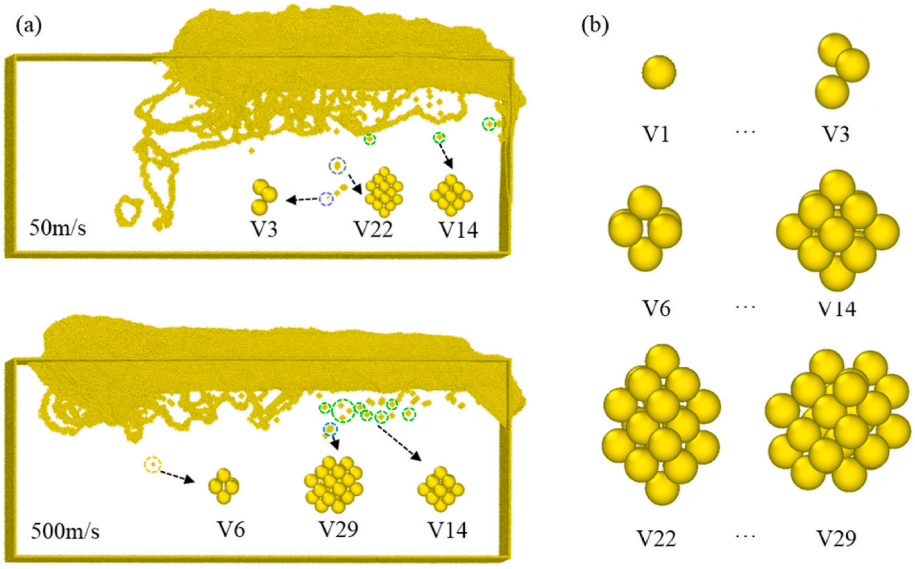

Fig. 10. (a) Snapshot of atomic clusters generated during the scratching process, (b) Illustration of structures of different atomic clusters.

face-centered cubic (FCC) or hexagonal close-packed (HCP) material systems, where stacking faults can be observed within the deformation zone, three-dimensional vacancy clusters are energetically favored in the BCC structure [42,43]. Therefore, atomic clusters rather than stacking faults are found in the subsurface layers in this simulation. The structures of different stable atomic clusters generated during scratching are illustrated in Fig. 10, where the VN-type atomic cluster contains N atoms. Beneath the workpiece, the V14-type vacancy clusters are most frequently observed after machining. These atomic clusters could be formed when the energetics reach a critical value, while the formation energies increase with the sizes of vacancy clusters [43]. Elimination of vacancy clusters could be achieved by annealing at high temperatures [44].

Fig. 11 illustrates the evolution of dislocations during nano-scratching at a speed of 200 m/s. Dislocations with Burgers vector of 1/2 <111>, <100>, and <110> are involved during the deformation process, while 1/2 <111> is the dominant dislocation type as the <111> directions are closely packed in the BCC structure. Corrugated dislocation lines are generated after scratching because 1/2 <111> dislocations have the potential to slide at different glide planes like {110}, {112}, and {123}, which causes cross-slip in the deformed region [45,46]. From Fig. 11(d), the dissociation and reorganization of 1/2<111> and <100> dislocations are observed in the subsurface of the workpiece, which follows the rules [47,48]:

$$1/2[11\bar{1}] + 1/2[1\bar{1}1] = [100], \tag{1}$$

$$[\bar{1}00] + 1/2[111] = 1/2[\bar{1}11], \tag{2}$$

Fig. 12 depicts the dislocation propagation in subsurface workpieces at various machining speeds. It is observed that the depth of dislocation extension is notably reduced as the machining speed increases to 500 m/s, which indicates localized plastic deformation near the machined surface corresponding to the “skin effect” at high machining speed. Additionally, separated 1/2<111> dislocation loops are present at machining speeds lower than 200 m/s. This characteristic can be explained that the 1/2<111> dislocation loops are thermodynamically unstable at high temperatures resulting from high machining speed [49].

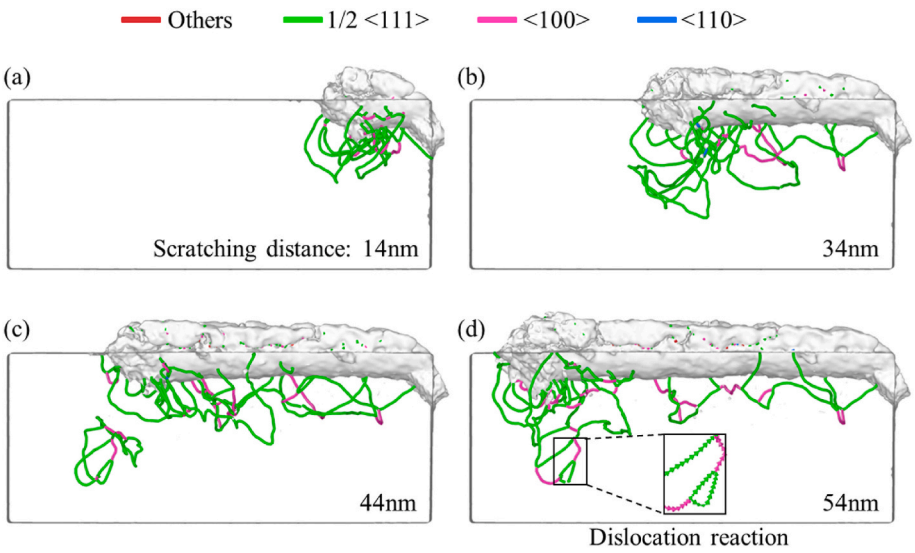

Fig. 11. The distribution of dislocations in the workpiece at a speed of 200 m/s with a scratching distance of (a) 14 nm, (b) 34 nm, (c) 44 nm, and (d) 54 nm.

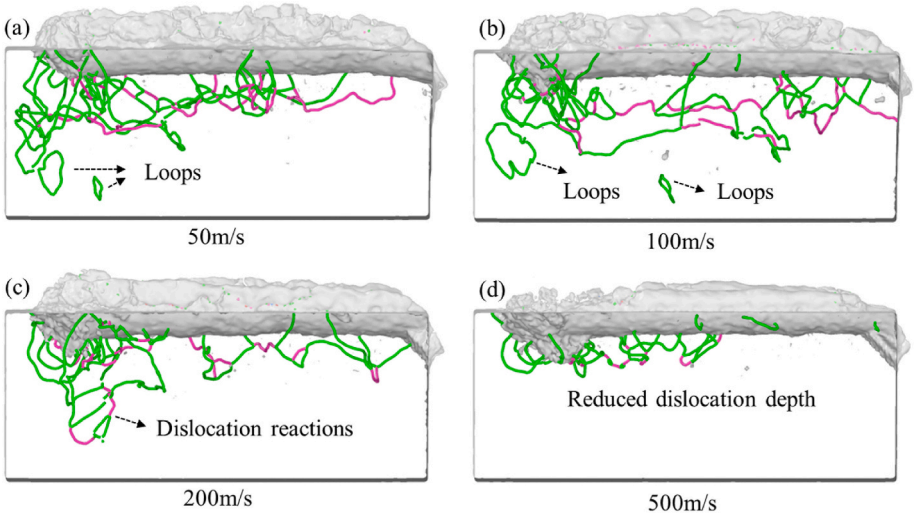

Fig. 12. The distribution of dislocations in the workpiece with a scratching distance of 54 nm at a speed of (a) 50 m/s, (b) 100 m/s, (c) 200 m/s, and (d) 500 m/s.

3.4. Stress and temperature analyses

For the machining process, analyzing the internal stress can provide insight into the local deformation of the subsurface workpiece [50]. The hydrostatic stress and von Mises stress could be obtained using the equations [21,51].

$$\sigma_{hydrostatic} = \frac{(\sigma_x + \sigma_y + \sigma_z)}{3}, \tag{3}$$

$$\sigma_{vonMises} = \sqrt{\frac{(\sigma_x\text{-}\sigma_y)^2 + (\sigma_y\text{-}\sigma_z)^2 + (\sigma_z\text{-}\sigma_x)^2 + 6\left(\tau_{xy}^2 + \tau_{yz}^2 + \tau_{zx}^2\right)}{2}}, \tag{4}$$

where σ_x, σ_y, σ_z, τ_{xy}, τ_{xz}, and τ_{yz} are stress tensors computed by LAMMPS. Figs. 13 and 14 present the cross-sectional view of the stress distribution as the scratching distance reaches 44 nm. As shown in Figs. 13 and 14, the compressive stress and von Mises stress are primarily localized near the tool during the scratching process while tensile stress can be observed behind the scratching tip due to tearing of the piled-up materials. On the machined surface, residual stresses are detected at low machining speeds. As the machining speed increases, the average stress in the deformation area decreases, as shown in Fig. 15. The decrease of the internal stress can be attributed to the recovery induced by high-rate release of strain energy during high-speed machining as the machining temperature increases. Residual stresses are released after the tool passes over the workpiece surface, especially when speeds reach up to 500 m/s. This observed stress relaxation could result from the annihilation of nucleated dislocations, which could influence the machining quality in the subsurface layer.

Temperature is another crucial factor that determines the material removal mechanisms as it significantly influences material properties [52,53]. Specifically, elevated temperatures can lead to phenomena such as softening, reduced elastic modulus, increased ductility, and enhanced atomic mobility. Furthermore, high temperature could facilitate the generation, movement, and annihilation of dislocations, which ultimately influence the deformation mechanisms within the material. For example, experimental work on high-speed grinding of silicon with different temperatures has shown that controlling the initial material temperature and achieving a critical grinding speed can influence the brittle-to-ductile transition in materials. Besides, the higher temperatures are thermally activated with higher kinetic energy to overcome the energy barrier and thus tend to form dislocations instead of cracks [53].

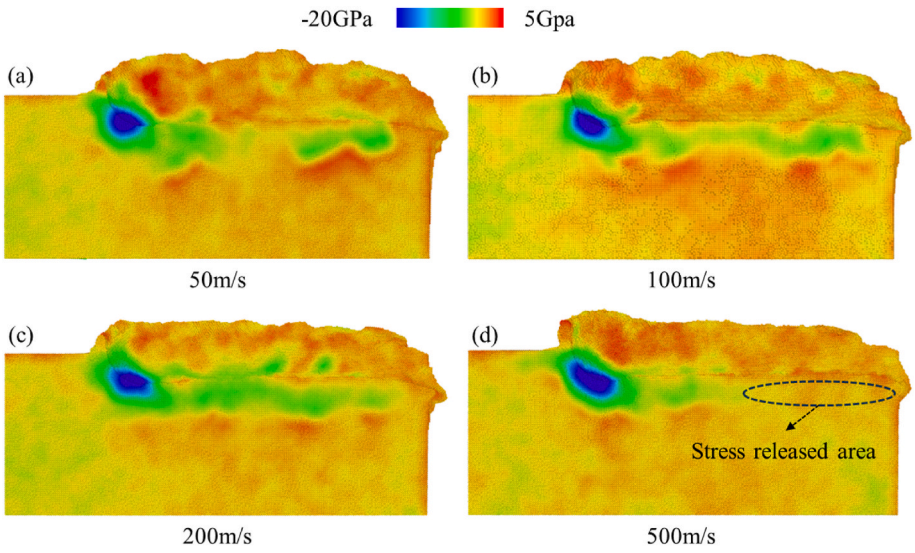

Fig. 13. The distribution of hydrostatic stress in the workpiece at a scratching distance of 44 nm with a speed of (a) 50 m/s, (b) 100 m/s, (c) 200 m/s, and (d) 500 m/s.

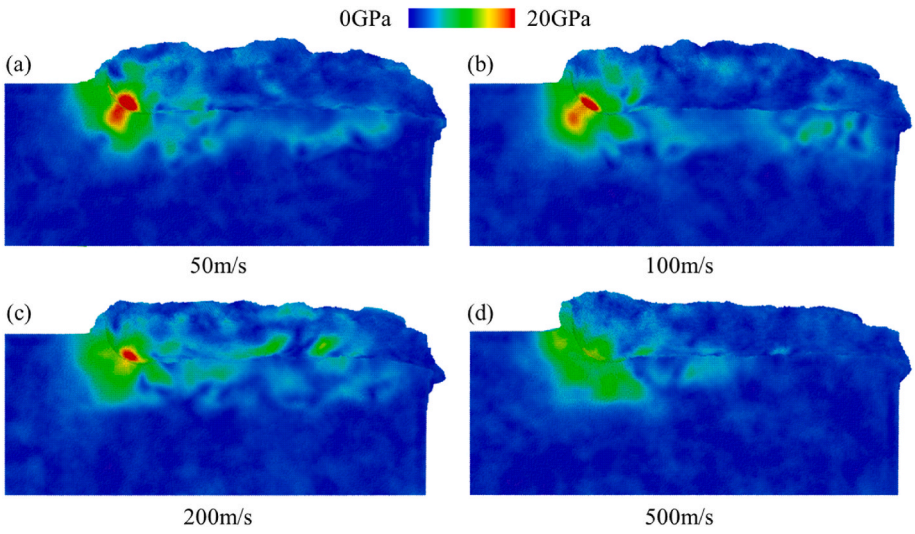

Fig. 14. The distribution of von Mises stress in the workpiece at a scratching distance of 44 nm with a speed of (a) 50 m/s, (b) 100 m/s, (c) 200 m/s, and (d) 500 m/s.

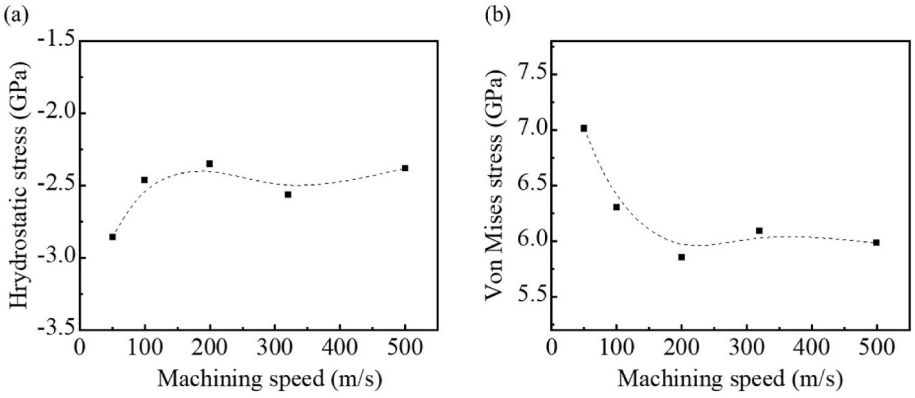

Fig. 15. Variation of average stress as a function of machining speed, (a) hydrostatic stress, and (b) von Mises stress.

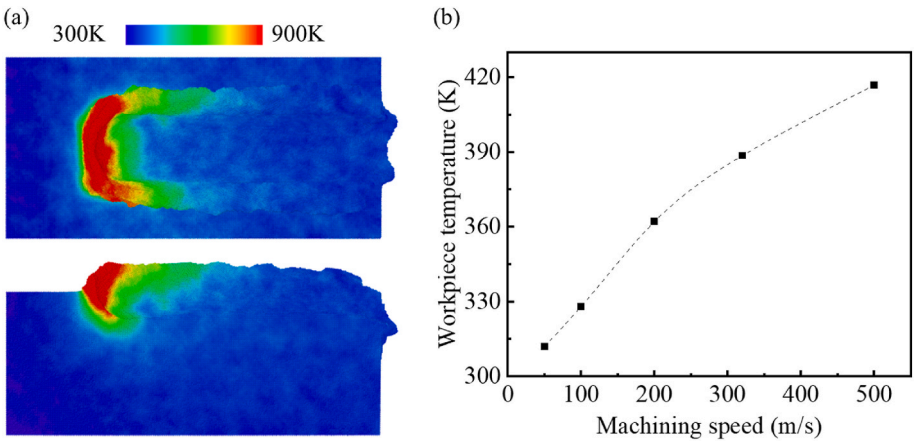

Fig. 16. (a) The temperature distribution of the workpiece at a scratching distance of 44 nm, (b) The workpiece temperature at various machining speeds.

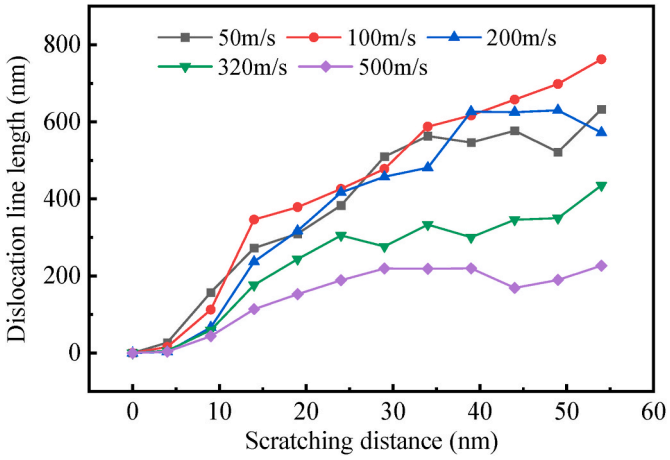

Fig. 17. Variation of dislocation length with machining speed at different scratching distances.

The temperature of atoms is calculated using the following equation

$$T = \langle \sum_{i=1}^{N} m_i v_i^2 \rangle \Big/ 3Nk_B, \tag{5}$$

where k_B is the Boltzmann constant and N represents atom number [54]. Fig. 16(a) illustrates the workpiece temperature distribution at a machining speed of 200 m/s. The high-temperature region is located in the high-pressure region and chip formation area. In MD simulation, the simulation is conducted in a vacuum environment and the thermal radiation is not considered in the energy transfer process. The generated heat is mainly dissipated by chips and thermostat groups of workpiece atoms. For a clear view of the temperature variation, the average workpiece temperatures under various machining speeds are calculated, as depicted in Fig. 16(b). With increasing machining speed, the workpiece temperature rises apparently as more kinetic energy is transferred into the workpiece.

4. Discussion

During the machining process, plastic deformation occurs with nucleation and movement of dislocations, forming a subsurface metamorphic layer in the workpiece. Variation of the total dislocation length with scratching distance is depicted in Fig. 17. As the scratching distance increases, the dislocation length increases along with the extension of the plastic deformation region. The increase of the dislocation length becomes less apparent as the scratching distance reaches 45 nm, as the dislocations reach the workpiece boundary. With increasing machining speed, the dislocation length decreases due to the localized plastic deformation. This phenomenon is consistent with the findings of Zheng et al. [55]. The decrease in the dislocation length at high machining speeds can be attributed to the high strain-rate effects and material embrittlement at ultra-high machining speeds [10]. During deformation, the coupling effect of temperature and strain rate plays a critical role in the evolution process of dislocations [56–58]. Previous studies have shown that the hardness and elastic properties of BCC metals are

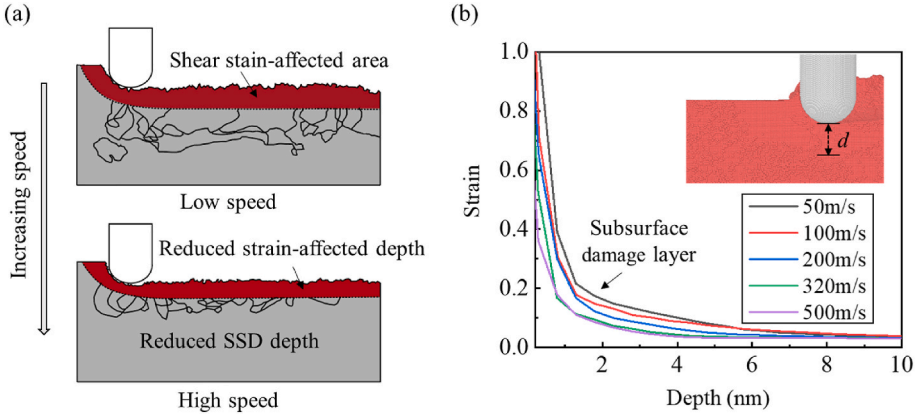

Fig. 18. (a) Schematic of shear strain-affected area and subsurface damage variation with machining speed, (b) the variation of strain as a function of depth from tool bottom at different machining speeds.

temperature-dependent, as well as the dislocation plasticity [57]. According to the thermal activation theory of dislocations, thermally activated atoms can more easily overcome energy barriers at elevated temperatures [59]. Choi et al. identified the thermally activated dislocation plasticity in BCC metals. They observed early-stage thermally activated dislocation plasticity, which aligns with the results of this study. Additionally, the model proposed by Lim et al. [60] illustrates the dependence of temperature and strain rate on the flow and yield surfaces of single crystals Fe. At low temperatures, the yield behavior of BCC metals primarily depends on the glide of 1/2<111> screw dislocations which necessitate moderate temperatures and stresses to overcome the typically high Peierls barrier [60]. At lower strain rates, dislocations can surmount obstacles and propagate continuously during plastic deformation. However, at higher speeds, the increase in strain rate causes temperature rise and insufficient time for dislocation slip, resulting in dislocation plugging and a subsequent reduction in material plasticity [39]. In summary, the temperature effect promotes dislocation evolution, while the high strain rate inhibits dislocation movement. As the velocity increases to 500 m/s, the deformation mechanism is mainly dominated by the strain rate effect rather than the temperature effect.

The interplay between thermal and mechanical effects plays an essential role in defining the characteristics of the machining-induced subsurface damage. Zhang et al. [11] proposed that the depth of the subsurface damage layer is proportionately related to the negative exponent of strain rate, and the empirical formula is expressed as

$$\delta = k \cdot \left(\frac{d\varepsilon}{dt}\right)^{-0.34}, \tag{6}$$

where k is a constant, and δ and $d\varepsilon/dt$ represent the depth of the subsurface damage layer and strain rate, respectively. The MD simulation results in this study identify a reduction in the depth of the deformation region at high machining speeds regarding the shear strain and dislocation activity. Fig. 18 (b) shows the decrease of shear strain as a function of depth from the cutting tool bottom at various machining speeds. The depth of the strain-affected layer decreases as the machining speed increases from 50 m/s to 500 m/s, which could contribute to the reduced subsurface damage depth in the workpiece at higher machining speeds. The same trend is also observed in the work from Luo et al. [61] and Zhang et al. [55], and they attributed this phenomenon to the shorter tool-workpiece interaction time, the more pronounced influence of the tool on the workpiece, and strain rate effects at higher cutting speeds. To further validate the deformation mechanisms observed in these simulations, such as dislocation activity and subsurface damage reduction at ultra-high speeds, controlled experimental studies across different machining speeds will be significant in the follow-up research to advance ultra-high-speed machining technology. Additionally, simulations suggest that combining low temperatures with high strain rates improves material removal efficiency and reduces subsurface damage for BCC metals, indicating that integrating cryogenic cooling [62] or minimum quantity lubrication (MQL) [63,64] has the potential to further optimize these outcomes.

5. Conclusions

In this study, MD simulations were conducted to examine the impact of machining speed on the deformation mechanisms of monocrystalline iron during nano-scratching. The surface generation, material removal process, and subsurface damage were analyzed and discussed. The key conclusions could be summarized below:

(1) A higher machining speed results in an elevated pile-up ratio and chip formation. Additionally, the shear strain is concentrated near the machined surface and diminishes along the depth direction, with its penetration depth decreasing as the machining speed increases.
(2) As the machining speeds increase from 50 m/s to 500 m/s, the temperature in the workpiece increases. The average tangential force and coefficient of friction (COF) initially decrease due to thermal softening up to 200 m/s, but increase at 500 m/s owing to the strain-hardening effect. Besides, the fluctuations in tangential force decrease with elevated machining speed, leading to a more consistent side flow pattern in the surface at 500 m/s.
(3) During the dislocation evolution process, 1/2<111> dislocation loops are generated at speeds lower than 200 m/s. The shortest dislocation length is observed at 500 m/s, which could be attributed to the strain rate effect dominating the deformation mechanisms at high machining speed.
(4) Compared with low machining speed at 50 m/s, the shear strain-affected depth and hydrostatic stress distribution area decrease obviously at 500 m/s, which could contribute to the reduced depth of the subsurface damage. This skin effect of machining damage indicates that ultra-high-speed machining has the potential to reduce subsurface damage.

In summary, this study offers atomic insights into the effect of machining speed on surface generation and subsurface evolution of iron. Based on the simulation results in this study, integrating ultra-high-speed machining with cryogenic cooling technology or a minimum quantity lubrication (MQL) system could further enhance material removal efficiency and reduce damage for BCC metals. Additionally, tool wear is an important aspect of the machining process that needs to be addressed. Diamond tool wear is closely related to the temperature of the machining area and the contact time between the tool and the workpiece. The reduction of the contact time under ultra-high-speed machining conditions gives it the potential to reduce tool wear, and it is meaningful to carry out experimental studies on tool wear in the future.

CRediT authorship contribution statement

Juan Chen: Writing – original draft, Visualization, Software, Methodology, Investigation, Formal analysis. **Changlin Liu:** Writing – review & editing, Software, Methodology, Formal analysis, Data curation. **Hao Liu:** Writing – review & editing, Validation, Formal analysis, Data curation. **Bi Zhang:** Writing – review & editing, Supervision, Resources, Formal analysis, Conceptualization. **Suet To:** Writing – review & editing, Supervision, Resources, Funding acquisition.

Declaration of competing interest

The authors declare that they have no known competing financial interests or personal relationships that could have appeared to influence the work reported in this paper.

Acknowledgments

The authors would like to thank the financial support from the Shenzhen Science and Technology Innovation Commission (grant nos. KQTD20190929172505711, GJHZ20210705141807023, JCYJ20210324115413036, JSGG20220831110605009) and Guangdong Basic and Applied Basic Research Foundation (2021B1515120009), and 2019JC01Z031. The authors also would like to thank the funding support from the State Key Laboratory of Ultra-precision Machining Technology of The Hong Kong Polytechnic University, and the Research Committee of The Hong Kong Polytechnic University (Project code: RJTX).

References

[1] Zhang S, To S, Zhang G. Diamond tool wear in ultra-precision machining. Int J Adv Manuf Technol 2016;88:613–41. https://doi.org/10.1007/s00170-016-8751-9.

[2] Yin T, Zhao T, Du H, Zhang G, Zhao Z, Hang W, et al. Investigation of forced wheel spindle vibration influence on surface formation in grinding of hard materials. Mech Syst Signal Process 2025;223:111921. https://doi.org/10.1016/j.ymssp.2024.111921.
[3] Jiang G, Jianguo Z, Yanan P, Renke K, Yoshiharu N, Paul S, et al. A critical review on the chemical wear and wear suppression of diamond tools in diamond cutting of ferrous metals. Int J Extrem Manuf 2020;2:012001. https://doi.org/10.1088/2631-7990/ab5d8f.
[4] Zou L, Yin J, Huang Y, Zhou M. Essential causes for tool wear of single crystal diamond in ultra-precision cutting of ferrous metals. Diam Relat Mater 2018;86:29–40. https://doi.org/10.1016/j.diamond.2018.04.012.
[5] Casstevens JM. Diamond turning of steel in carbon-saturated atmospheres. Precis Eng 1983;5:9–15. https://doi.org/10.1016/0141-6359(83)90063-6.
[6] Evans C, Bryan JB. Cryogenic diamond turning of stainless steel. CIRP Ann 1991;40:571–5. https://doi.org/10.1016/S0007-8506(07)62056-3.
[7] Brinksmeier E, Gläbe R, Osmer J. Ultra-precision diamond cutting of steel molds. CIRP Ann 2006;55:551–4. https://doi.org/10.1016/S0007-8506(07)60480-6.
[8] Moriwaki T, Shamoto E. Ultraprecision diamond turning of stainless steel by applying ultrasonic vibration. CIRP Ann 1991;40:559–62. https://doi.org/10.1016/S0007-8506(07)62053-8.
[9] Zhang X, Liu K, Kumar A, Rahman M. A study of the diamond tool wear suppression mechanism in vibration-assisted machining of steel. J Mater Process Technol 2014;214:496–506. https://doi.org/10.1016/J.JMATPROTEC.2013.10.002.
[10] Yang X, Zhang B. Material embrittlement in high strain-rate loading. Int J Extrem Manuf 2019;1:022003. https://doi.org/10.1088/2631-7990/ab263f.
[11] Zhang B, Yin J. The 'skin effect' of subsurface damage distribution in materials subjected to high-speed machining. Int J Extrem Manuf 2019;1:012007. https://doi.org/10.1088/2631-7990/ab103b.
[12] Guo S, Zhang J, Jiang Q, Zhang B. Surface integrity in high-speed grinding of Al6061T6 alloy. CIRP Ann 2022;71:281–4. https://doi.org/10.1016/j.cirp.2022.03.002.
[13] Li P, Jin T, Xiao H, Chen Z, Qu M, Dai H, et al. Effects of wheel speed on surface/subsurface damage characteristics in grinding of glass-ceramics. Ceram Int 2020;46:17717–28. https://doi.org/10.1016/j.ceramint.2020.04.076.
[14] Guo S, Lu S, Zhang B, Cheung CF. Surface integrity and material removal mechanisms in high-speed grinding of Al/SiCp metal matrix composites. Int J Mach Tool Manufact 2022;178:103906. https://doi.org/10.1016/j.ijmachtools.2022.103906.
[15] Yang J, Wang X, Kang M. Finite element simulation of surface roughness in diamond turning of spherical surfaces. J Manuf Process 2018;31:768–75. https://doi.org/10.1016/j.jmapro.2018.01.006.
[16] Veiga RGA, Goldenstein H, Perez M, Becquart CS. Monte Carlo and molecular dynamics simulations of screw dislocation locking by Cottrell atmospheres in low carbon Fe–C alloys. Scripta Mater 2015;108:19–22. https://doi.org/10.1016/j.scriptamat.2015.06.012.
[17] Goel S, Kovalchenko A, Stukowski A, Cross G. Influence of microstructure on the cutting behaviour of silicon. Acta Mater 2016;105:464–78. https://doi.org/10.1016/j.actamat.2015.11.046.
[18] Liu C, Chen X, Ke J, She Z, Zhang J, Xiao J, et al. Numerical investigation on subsurface damage in nanometric cutting of single-crystal silicon at elevated temperatures. J Manuf Process 2021;68:1060–71. https://doi.org/10.1016/j.jmapro.2021.06.040.
[19] Fan Y, Wang W, Hao Z, Zhan C. Work hardening mechanism based on molecular dynamics simulation in cutting Ni–Fe–Cr series of Ni-based alloy. J Alloys Compd 2020;819:153331. https://doi.org/10.1016/j.jallcom.2019.153331.
[20] Chen C, Lai M, Fang F. Subsurface deformation mechanism in nano-cutting of gallium arsenide using molecular dynamics simulation. Nanoscale Res Lett 2021;16:117. https://doi.org/10.1186/s11671-021-03574-3.
[21] Li J, Fang Q, Zhang L, Liu Y. Subsurface damage mechanism of high speed grinding process in single crystal silicon revealed by atomistic simulations. Appl Surf Sci 2015;324:464–74. https://doi.org/10.1016/j.apsusc.2014.10.149.
[22] Li P, Guo X, Yuan S, Li M, Kang R, Guo D. Effects of grinding speeds on the subsurface damage of single crystal silicon based on molecular dynamics simulations. Appl Surf Sci 2021;554:149668. https://doi.org/10.1016/j.apsusc.2021.149668.
[23] Zhang JQ, He BB, Zhang B. On the transition of failure mechanisms during machining process with varied speeds: a molecular dynamics study. J Manuf Process 2023;106:537–51. https://doi.org/10.1016/j.jmapro.2023.09.064.
[24] Zhao P, Zhao B, Pan J, Wu J. Nano-grinding process of single-crystal silicon using molecular dynamics simulation: nano-grinding parameters effect. Mater Sci Semicond Process 2022;143:106531. https://doi.org/10.1016/j.mssp.2022.106531.
[25] Li J, Fang Q, Liu Y, Zhang L. A molecular dynamics investigation into the mechanisms of subsurface damage and material removal of monocrystalline copper subjected to nanoscale high speed grinding. Appl Surf Sci 2014;303:331–43. https://doi.org/10.1016/j.apsusc.2014.02.178.
[26] Plimpton S. Fast Parallel algorithms for short-range molecular dynamics. J Comput Phys 1995;117:1–19. https://doi.org/10.1006/jcph.1995.1039.
[27] Stukowski A. Visualization and analysis of atomistic simulation data with OVITO–the Open Visualization Tool. Model Simulat Mater Sci Eng 2009;18:015012. https://doi.org/10.1088/0965-0393/18/1/015012.
[28] Shinoda W, Shiga M, Mikami M. Rapid estimation of elastic constants by molecular dynamics simulation under constant stress. Phys Rev B 2004;69:134103. https://doi.org/10.1103/PhysRevB.69.134103.
[29] Gao Y, Urbassek HM. Evolution of plasticity in nanometric cutting of Fe single crystals. Appl Surf Sci 2014;317:6–10. https://doi.org/10.1016/j.apsusc.2014.08.020.
[30] Huang W, Tang J, Zhou W, Wen J, Yi M. Molecular dynamics simulations of ultrasonic vibration-assisted grinding of polycrystalline iron: nanoscale plastic deformation mechanism and microstructural evolution. Appl Surf Sci 2023:158440. https://doi.org/10.1016/j.apsusc.2023.158440.
[31] Banerjee S, Naha S, Puri IK. Molecular simulation of the carbon nanotube growth mode during catalytic synthesis. Appl Phys Lett 2008;92:233121. https://doi.org/10.1063/1.2945798.
[32] Mendelev MI, Han S, Srolovitz DJ, Ackland GJ, Sun DY, Asta M. Development of new interatomic potentials appropriate for crystalline and liquid iron. Philos Mag A 2003;83:3977–94. https://doi.org/10.1080/14786430310001613264.
[33] Huang W, Tang J, Zhou W, Shao W, Yi M, Zhao X, et al. Revealing nanoscale material deformation mechanism and surface/subsurface characteristics in vibration-assisted nano-grinding of single-crystal iron. Appl Surf Sci 2022;597:153692. https://doi.org/10.1016/j.apsusc.2022.153692.
[34] Liu C, Zhuang Z, Chen J, Yip WS, To S. Atomic-scale investigation of Pt composition on deformation mechanism of AuPt alloy during nano-scratching process. Surface Interfac 2023;40:103126. https://doi.org/10.1016/j.surfin.2023.103126.
[35] Ren J, Lai M, Fang F. Surface morphology of polycrystalline cerium–lanthanum alloy in nanometric cutting. J Manuf Process 2023;101:714–20. https://doi.org/10.1016/j.jmapro.2023.05.111.
[36] Wang Y, Tang S, Guo J. Molecular dynamics study on deformation behaviour of monocrystalline GaN during nano abrasive machining. Appl Surf Sci 2020;510:145492. https://doi.org/10.1016/j.apsusc.2020.145492.
[37] Chavoshi SZ, Goel S, Luo X. Molecular dynamics simulation investigation on the plastic flow behaviour of silicon during nanometric cutting. Model Simulat Mater Sci Eng 2015;24:015002. https://doi.org/10.1088/0965-0393/24/1/015002.
[38] Wu C-D, Fang T-H, Sung P-H, Hsu Q-C. Critical size, recovery, and mechanical property of nanoimprinted Ni–Al alloys investigation using molecular dynamics simulation. Comput Mater Sci 2012;53:321–8. https://doi.org/10.1016/j.commatsci.2011.09.027.
[39] Tian L, Fu Y, Xu J, Li H, Ding W. The influence of speed on material removal mechanism in high speed grinding with single grit. Int J Mach Tool Manufact 2015;89:192–201. https://doi.org/10.1016/j.ijmachtools.2014.11.010.
[40] Yip WS, To S. Reduction of material swelling and recovery of titanium alloys in diamond cutting by magnetic field assistance. J Alloys Compd 2017;722:525–31. https://doi.org/10.1016/j.jallcom.2017.06.167.
[41] Wang Q, Bai Q, Chen J, Sun Y, Guo Y, Liang Y. Subsurface defects structural evolution in nano-cutting of single crystal copper. Appl Surf Sci 2015;344:38–46. https://doi.org/10.1016/j.apsusc.2015.03.061.
[42] Ma P-W, Mason DR, Dudarev SL. Multiscale analysis of dislocation loops and voids in tungsten. Phys Rev Mater 2020;4:103609. https://doi.org/10.1103/PhysRevMaterials.4.103609.
[43] Hou J, You Y-W, Kong X-S, Song J, Liu CS. Accurate prediction of vacancy cluster structures and energetics in bcc transition metals. Acta Mater 2021;211:116860. https://doi.org/10.1016/j.actamat.2021.116860.
[44] Konstantinović MJ, Bonny G. Thermal stability and the structure of vacancy–solute clusters in iron alloys. Acta Mater 2015;85:107–11. https://doi.org/10.1016/j.actamat.2014.11.026.
[45] Weinberger CR, Boyce BL, Battaile CC. Slip planes in bcc transition metals. Int Mater Rev 2013;58:296–314. https://doi.org/10.1179/1743280412Y.0000000015.
[46] Franciosi P, Le LT, Monnet G, Kahloun C, Chavanne M-H. Investigation of slip system activity in iron at room temperature by SEM and AFM in-situ tensile and compression tests of iron single crystals. Int J Plast 2015;65:226–49. https://doi.org/10.1016/j.ijplas.2014.09.008.
[47] Chou YT. Dislocation energy and dislocation networks in α-iron. J Appl Phys 1965;36:1435–8. https://doi.org/10.1063/1.1714324.
[48] Yamanaka A, McReynolds K, Voorhees PW. Phase field crystal simulation of grain boundary motion, grain rotation and dislocation reactions in a BCC bicrystal. Acta Mater 2017;133:160–71. https://doi.org/10.1016/j.actamat.2017.05.022.
[49] Dudarev SL, Bullough R, Derlet PM. Effect of the α-γ phase transition on the stability of dislocation loops in bcc iron. Phys Rev Lett 2008;100:135503. https://doi.org/10.1103/PhysRevLett.100.135503.
[50] Cross GLW. Isolation leads to change. Nat Nanotechnol 2011;6:467–8. https://doi.org/10.1038/nnano.2011.124.
[51] Dai H, Zhou Y, Zhang F. Atomistic simulation of influence of laser nano-structured diamond abrasive on the polishing behavior of silicon. Mater Sci Semicond Process 2020;105:104706. https://doi.org/10.1016/j.mssp.2019.104706.
[52] Chavoshi SZ, Goel S, Luo X. Influence of temperature on the anisotropic cutting behaviour of single crystal silicon: a molecular dynamics simulation investigation. J Manuf Process 2016;23:201–10. https://doi.org/10.1016/j.jmapro.2016.06.009.
[53] Zhang J, Shang X, He B, Zhang B. Towards understanding the crack suppression mechanism in brittle materials with high grinding speed at different temperatures. Int J Mach Tool Manufact 2023:104088. https://doi.org/10.1016/j.ijmachtools.2023.104088.
[54] Guo Y, Liang Y, Chen M, Bai Q, Lu L. Molecular dynamics simulations of thermal effects in nanometric cutting process. Sci China Technol Sci 2010;53:870–4. https://doi.org/10.1007/s11431-009-0243-9.
[55] Zheng J, Zhang G, Zhang W, Huang Z, Lai Z. Generation mechanism of optical surface in ultra-precision cutting polycrystalline zinc selenide. Appl Surf Sci 2024;676:161005. https://doi.org/10.1016/j.apsusc.2024.161005.

[56] Beyerlein IJ, Tomé CN. A dislocation-based constitutive law for pure Zr including temperature effects. Int J Plast 2008;24:867–95. https://doi.org/10.1016/j.ijplas.2007.07.017.
[57] Choi I-C, Brandl C, Schwaiger R. Thermally activated dislocation plasticity in body-centered cubic chromium studied by high-temperature nanoindentation. Acta Mater 2017;140:107–15. https://doi.org/10.1016/j.actamat.2017.08.026.
[58] Malyar NV, Dehm G, Kirchlechner C. Strain rate dependence of the slip transfer through a penetrable high angle grain boundary in copper. Scripta Mater 2017;138:88–91. https://doi.org/10.1016/j.scriptamat.2017.05.042.
[59] Meyers MA, Benson DJ, Vöhringer O, Kad BK, Xue Q, Fu H-H. Constitutive description of dynamic deformation: physically-based mechanisms. Mater Sci Eng, A 2002;322:194–216. https://doi.org/10.1016/S0921-5093(01)01131-5.
[60] Lim H, Hale LM, Zimmerman JA, Battaile CC, Weinberger CR. A multi-scale model of dislocation plasticity in α-Fe: incorporating temperature, strain rate and non-Schmid effects. Int J Plast 2015;73:100–18. https://doi.org/10.1016/j.ijplas.2014.12.005.
[61] Fan P, Goel S, Luo X, Yan Y, Geng Y, He Y. Origins of ductile plasticity in a polycrystalline gallium arsenide during scratching: MD simulation study. Appl Surf Sci 2021;552:149489. https://doi.org/10.1016/j.apsusc.2021.149489.
[62] Hribersek M, Pusavec F, Rech J, Kopac J. Modeling of machined surface characteristics in cryogenic orthogonal turning of inconel 718. Mach Sci Technol 2018;22(5):829–50. https://doi.org/10.1080/10910344.2017.1415935.
[63] Khatai S, Kumar R, Panda A, Sahoo AK. WASPAS based multi response optimization in hard turning of AISI 52100 steel under ZnO nanofluid assisted dual nozzle pulse-MQL environment. Appl Sci 2023;13:10062. https://doi.org/10.3390/app131810062.
[64] Khatai S, Kumar Sahoo A, Kumar R, Panda A. On Machining behaviour of various cutting Inserts: a review on hardened steel. Mater Today Proc 2022;62:3485–92. https://doi.org/10.1016/j.matpr.2022.04.301.